Inorganic Chemistry
Article

Inorg. Chem. **2010**, *49*, 1587–1594 **1587**
DOI: 10.1021/ic9019876

Crystal Structure and Optical and Magnetic Properties of $Pr_2(MoO_4)_3$

D. Logvinovich,*,† A. Arakcheeva,† P. Pattison,†,‡ S. Eliseeva,§ P. Tomeš,∥ I. Marozau,⊥ and G. Chapuis†

†*École Polytechnique Fédérale de Lausanne, Laboratoire de Cristallographie, BSP-Cubotron, CH-1015 Lausanne, Switzerland,* ‡*Swiss-Norwegian Beamline, ESRF, BP-220, F-38043 Grenoble CEDEX, France,* §*École Polytechnique Fédérale de Lausanne, Laboratory of Lanthanide Supramolecular Chemistry, BCH 1405, CH-1015 Lausanne, Switzerland,* ∥*EMPA, Solid State Chemistry and Catalysis, Ueberlandstrasse 129, CH-8600 Duebendorf, Switzerland, and* ⊥*Department of General Energy Research, Paul Scherrer Institut, 5232 Villigen PSI, Switzerland*

Received October 7, 2009

Praseodymium molybdate $Pr_2(MoO_4)_3$ was synthesized using the standard ceramic route. The crystal structure of the material has been successfully solved in superspace group $I2/b(\alpha\beta0)00$ with lattice constants a = 5.30284(4), b = 5.32699(3), c = 11.7935(1) Å, γ = 90.163(1)°, and the modulation vector $\mathbf{q} = 2/3\mathbf{a}^* + 0.88810(2)\mathbf{b}^*$. The deviation of the **q** vector from a rational value allows a description of the structure in terms of nanosize domains with the $La_2(MoO_4)_3$-like structure separated by stacking faults. Under 450 nm excitation, ($^3P_0$ level) $Pr_2(MoO_4)_3$ exhibits the characteristic red emission, with the most intense band at 649 nm corresponding to a $^3P_0 \rightarrow {}^3F_2$ transition. Magnetic susceptibility measurements reveal Curie−Weiss paramagnetism with predominating antiferromagnetic interactions between Pr^{3+}-magnetic moments and no evidence of magnetic transitions down to T = 5 K.

Introduction

Oxides with scheelite-related structures have been extensively investigated during the past four decades, owing to their interesting physical properties.[1−8] The basic undistorted scheelite-related AXO_4 crystal structure consists of edge-sharing AO_8 polyhedra linked to XO_4 tetrahedra by common vertices (Figure 1). Each A and X cation is surrounded by eight and four oxygen ions, respectively, whereas each O^{2-} ion is surrounded by two A and one X cation. This structure can tolerate a number of cationic substitutions, which can be expressed by the general formula $(A', A'')_{n-\delta A}[(X', X'')O_4]_{n-\delta X}$, where A′(A″) and X′(X″) represent atoms occupying A and X positions, respectively, and $\delta A \geq 0$ and $\delta X \geq 0$ define vacancies on the corresponding sites. Typically, A is alkaline, alkaline-earth, or rare earth, and X = Mo, W, or V. Due to a large number of possible cationic substitutions and possible polymorphism, the spectrum of physical properties displayed by scheelites is very broad. Applications have been found in various optoelectronic fields such as solid-state lasers,[7,9] scintillators,[4,10] Raman shifters,[11,12] phosphors,[8] and so forth.

Although a number of useful applications are already known for scheelites, the crystal structures of many of them, a key for designing materials with certain physical properties, still present some puzzling challenges.[13] Scheelites with mixed occupied cationic sites preserve at least eight types of different ordered anion distributions. X-ray powder diffractograms of some of the ordered scheelites together with the main structure often contain weak additional reflections. These reflections cannot be indexed on the basis of the unit cells and are therefore often neglected or assigned to impurity phases. A recent electron diffraction study on $KNd(MoO_4)_2$[14] and $KSm(MoO_4)_2$[15] revealed similar reflections on X-ray powder

*To whom correspondence should be addressed. E-mail: dmitry.logvinovich@epfl.ch.

(1) Borchardt, H. J.; Bierstedt, P. E. *J. Appl. Phys.* **1967**, *38*, 2057–2060.
(2) Gorobets, B. S.; Mikhalev, A. A.; Nauchitel, M. A. *J. Appl. Spectrosc.* **1976**, *25*, 918–920.
(3) Hanuza, J.; Macalik, L. *Spectrochim. Acta, Part A* **1982**, *38*, 61–72.
(4) Kobayashi, M.; Ishii, M.; Usuki, Y.; Yahagi, H. *Nucl. Instrum. Methods Phys. Res., Sect. A* **1993**, *333*, 429–433.
(5) Macalik, L.; Hanuza, J.; Sokolnicki, J.; Legendziewicz, J. *J. Appl. Spectrosc.* **1995**, *62*, 832–839.
(6) Basiev, T. T.; Sobol, A. A.; Voronko, Y. K.; Zverev, P. G. *Opt. Mater.* **2000**, *15*, 205–216.
(7) Kaminskii, A. A. *Phys. Status Solidi A* **2003**, *200*, 215–296.
(8) Su, Y.; Li, L.; Li, G. *Chem. Mater.* **2008**, *20*, 6060–6067.
(9) Kaminskii, A.; Sarkiso, S. E.; Pavlyuk, A. V. L. *Izv. Akad. Nauk. SSSR, Neorg. Mater.* **1980**, *16*, 501.
(10) Baryshevsky, V. G.; Korzhik, M. V.; Moroz, V. I.; Pavlenko, V. B.; Lobko, A. S.; Fyodorov, A. A.; Kachanov, V. A.; Solovjanov, V. L.; Zadneprovsky, B. I.; Nefyodov, V. A.; Nefyodov, P. V.; Dorogovin, B. A.; Nagornaja, L. L. *Nucl. Instrum. Methods Phys. Res., Sect. A* **1992**, *322*, 231–234.
(11) Zverev, P. G.; Basiev, T. T.; Prokhorov, A. M. *Opt. Mater.* **1999**, *11*, 335–352.
(12) Cerny, P.; Jelinkova, H.; Basiev, T. T.; Zverev, P. G. *Quantum Electron.* **2002**, *38*, 1471–1478.
(13) Arakcheeva, A.; Chapuis, G. *Acta Crystallogr., Sect. B: Struct. Sci.* **2008**, *64*, 12–25.
(14) Morozov, V. A.; Arakcheeva, A. V.; Chapuis, G.; Guiblin, N.; Rossell, M. D.; VanTendeloo, G. *Chem. Mater.* **2006**, *18*, 4075–4082.
(15) Arakcheeva, A.; Pattison, P.; Chapuis, G.; Rossell, M.; Filaretov, A.; Morozov, V.; Van Tendeloo, G. *Acta Crystallogr., Sect. B: Struct. Sci.* **2008**, *64*, 160–171.

Published on Web 01/12/2010

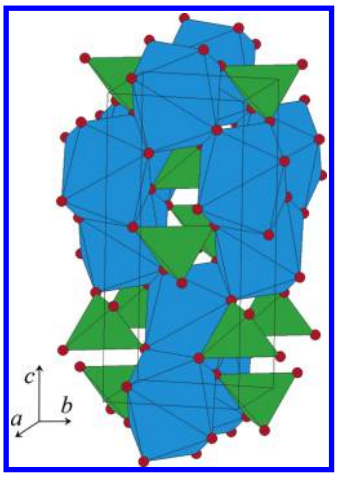

Figure 1. Crystal structure of scheelite viewed along the [010] direction: AO_8 and XO_4 polyhedra are shown with blue and green colors, respectively.

diffractograms which could be interpreted as satellite reflections resulting from incommensurate phases. Further studies led to the derivation of the crystal structure model based on the superspace group $I2/b(\alpha\beta0)00$, which allowed indexing of their diffraction patterns and refinement of their structures along with some other scheelites with cations or vacancies ordered in the *ab* plane.[13] The presence of satellite reflections was explained in terms of composition waves resulting from a two-component modulation vector **q**, the lengths of which are incommensurate with the lattice periodicity. It appears that the application of the superspace approach is a key factor in obtaining detailed information on the structural characteristics of members of the scheelite family in order to link them to their physical properties.

Special considerations have been dedicated to those rare earths containing scheelites, which emit in the visible or infrared regions of the electromagnetic spectrum because of their possible applications in luminescent and telecommunication devices.[16−18] Among rare earths, the Pr^{3+} ion is known for its rich emission spectrum with characteristic f−f transitions in the visible ($^3P_0 \rightarrow {}^3H_J$, ^3F_J, $^1D_2 \rightarrow {}^3H_J$) as well as in the near-infrared ranges ($^1D_2 \rightarrow {}^3F_4$, $^1G_4$).[19] In particular, its red emission is interesting for application in white light-emitting diodes (LEDs),[17] and the near-infrared region is interesting for telecommunication devices.[16] Therefore, luminescence properties and crystal structures of a number of Pr-containing scheelite oxides have been studied.[5,20−22] It has to be noted that retaining the valence state of the Pr ion is of importance since the presence of Pr^{4+} ions can significantly deteriorate the emission properties of the material.[23] Since the scheelite oxides are of particular interest, here, we consider the crystal structure and optical and magnetic properties of praseodymium molybdate, $Pr_2(MoO_4)_3$, related to a scheelite family, where 1/3 of the A-site positions are vacant.[1,24,25]

Experimental Section

A total of 2 g of $Pr_2(MoO_4)_3$ was prepared from stoichiometric amounts of Pr_6O_{11} (99.99%, Alfa Aesar) and MoO_3 (> 99.5%, Alfa Aesar) by the standard ceramic route. Before weighting, Pr_6O_{11} was annealed at $T = 1223$ K overnight to remove excessive moisture and carbon dioxide. The starting oxides were thoroughly mixed with acetone in an agate mortar and reacted at temperatures of 753, 803, and 1223 K over 24, 160, and 15 h, respectively, yielding a green-colored $Pr_2(MoO_4)_3$. Heating and cooling rates were 10 and 1 K/min, respectively.

The data set used to index the diffraction pattern was collected at $T = 298$ K in the angular range of $2\Theta = 5-40°$ using a Phillips X'Pert PRO MPD Θ−Θ X-ray powder diffractometer equipped with an X'Celerator linear detector and a graphite secondary monochromator. The sample was placed into a deep-load sample holder. The measurement was done in the reflection mode with a step size of 0.008°, a counting time of 1500 s/point, Cu $K\alpha_1/K\alpha_2$ radiation, a goniometer radius of 240 mm, 0.02 rad primary soller slits, a 1/4° receiving slit, and a 15 mm mask. A total of 25 single reflections were resolved in the angular range of $2\Theta = 10.05-30.33°$. Each reflection was fitted with a pseudo-Voigt profile function using X'Pert HighScore Plus software from Phillips. The correction for the 2Θ offset (−0.01°) was determined from the preliminary measurement made on a $Pr_2(MoO_4)_3$ sample admixed with 10 wt % of the line position standard Mica SRM 675. The mixture was applied on a silicon sample holder using ethanol to avoid the preferred orientation of the standard. For calibration, the positions of the four first lines of the standard were used. Indexing was performed with zone-searching and successive dichotomy methods implemented in the software *ITO12*[26] and *DICVOL06*,[27] a part of *CRYSFIRE*[28] indexing suite. The best solution for the space group was selected using the program *CHECKCELL*.[29]

The room-temperature powder diffraction experimental data sets used for the Rietveld refinement were collected with two instruments. One data set was collected with a Mar-Research MAR345 image-plate area detector using synchrotron radiation on beamline BM01A (SNBL) at the ESRF, Grenoble ($\lambda = 0.7092$ Å, Si(111) monochromator and focusing mirrors). The diffraction pattern was collected at a sample−detector distance of 200 mm. The sample was placed in a 0.5-mm-diameter capillary, which was rotated through 30° during an exposure of 30 s per image. The collected data had a good signal-to-noise ratio but a moderate resolution. Another pattern was collected using a Phillips X'Pert powder diffractometer. The experimental setup and measurement conditions were essentially the same as for the indexing except for the angular range ($2\Theta = 5.0-150.0°$). The collected data had a worse signal-to-noise ratio compared to the

(16) Naftaly, M.; Jha, A.; Jordan, W. G. *J. Appl. Phys.* **1998**, *84*, 1800–1804.
(17) Ronda, C. R.; Justel, T.; Nikol, H. *J. Alloys Compd.* **1998**, *275−277*, 669–676.
(18) Ronda, C. *Luminescence: From Theory to Applications*; Wiley-VCH: Weinheim, Germany, 2008.
(19) Bünzli, J.-C. G.; Eliseeva, S. V. *Lanthanide Spectroscopy, Materials and Bio-applications*; Springer Verlag: Berlin, 2010; Vol. 7.
(20) Köstler, W.; Winnacker, A.; Rossner, W.; Grabmaier, B. C. *J. Phys. Chem. Solids* **1995**, *56*, 907–913.
(21) Gaft, M.; Reisfeld, R.; Panczer, G.; Uspensky, E.; Varrel, B.; Boulon, G. *Opt. Mater.* **1999**, *13*, 71–79.
(22) Jouini, A.; Gacon, J. C.; Ferid, M.; Trabelsi-Ayadi, M. *Opt. Mater.* **2003**, *24*, 175–180.
(23) Pawlak, D.; Frukacz, Z.; Mierczyk, Z.; Suchocki, A.; Zachara, J. *J. Alloys Compd.* **1998**, *275−277*, 361–364.
(24) Nassau, K.; Levinstein, H. J.; Loiacono, G. M. *J. Phys. Chem. Solids* **1965**, *26*, 1805–1816.
(25) Jamieson, P. B.; Abrahams, S. C.; Bernstein, J. L. *J. Chem. Phys.* **1969**, *50*, 86–94.
(26) Visser, J. W. *J. Appl. Crystallogr.* **1969**, *2*, 89–95.
(27) Boultif, A.; Louer, D. *J. Appl. Crystallogr.* **2004**, *37*, 724–731.
(28) Shirley, R. *NBS Spec. Publ.* **1980**, *567*, 361−382.
(29) Laugier, J.; Bochu, B. *LMGP Suite for Windows*; Laboratoire des Matériaux et du Génie Physique de l'Ecole Nationale Supérieure de Physique de Grenoble: Grenoble, France. Available at http://www.inpg.fr/LMGP and http://www.ccp14.ac.uk/tutorial/lmgp/ (accessed Jan 2010).

Table 1. Details on the $Pr_2(MoO_4)_3$ Structure Refinement Using the Superspace Model

Crystal Data		
chemical formula	$Pr_2(MoO_4)_3$	
M_r	761.63	
cell setting, space group	monoclinic, $I2/b(\alpha\beta0)00$	
temperature (K)	298	
a, b, c (Å)	5.30284(4), 5.32699(3), 11.7935(1)	
γ (deg)	90.163(1)	
V, Å^3	333.14(1)	
Z	7	
D_x (Mg m^{-3})	5.0600(1)	
μ (mm^{-1})	13.05	103.99
modulation wavevector	$\mathbf{q} = 2/3\mathbf{a}^* + 0.88810(2)\mathbf{b}^*$	
radiation type	synchrotron	Cu $K\alpha_1/K\alpha_2$
specimen form, color	capillary, green	cylinder, green
specimen size (mm)	0.3	
absorption correction μr	0.67	none
specimen preparation cooling	cooling from 1023 to 298 K with 1 K/min in the air	
specimen preparation pressure (kPa)	101.325	
specimen preparation temperature (K)	298	
Data Collection		
diffractometer	MAR345	Phillips X'Pert PRO MPD $\theta-\theta$
data collection method	specimen mounting, glass capillary; mode, transmission	specimen mounting, infinite thickness sample holder; mode, reflection
2θ (deg)	4−34.2	5−150
Refinement		
overall R factors and goodness of fit	$R_p = 0.0481$, $wR_p = 0.0660$, $S = 1.99$	
wavelength of incident radiation (Å)	0.7089	1.540598/1.544426
excluded region(s)	none	
profile function	pseudo-Voigt	
no. of params/no. of reflns	72/25200	
weighting scheme	based on measured s.u.'s	
$(\Delta/\sigma)_{max}$	0.05	

synchrotron data set but had better resolution. The refinement was performed on the basis of these two data sets.

Crystal structure refinements were performed using the software *JANA2006*.[30] All of the figures were obtained from the *JANA2006* and *DIAMOND*[31] program packages.

Optical properties of the polycrystalline powder were investigated by diffuse reflectance spectroscopy. Reflectance data were collected at $T = 298$ K using a Varian Cary 500 Scan UV−vis−NIR scanning double-beam spectrometer equipped with a 150 mm Lambdasphere DRA-CA-50 integrating sphere over the spectral range of 250−800 nm.

Luminescence data were recorded with a Fluorolog FL3-22 spectrofluorimeter from Horiba-Jobin-Yvon Ltd. on well-ground powder samples placed in quartz capillaries with an internal diameter of 2.4 mm. Lifetimes were measured upon the excitation of the Pr^{3+} ion ($^3P_2$ level, 450 nm) and monitoring the $^3P_0 \rightarrow {}^3F_2$ transition. Luminescence decays were analyzed with Origin and proved to be single-exponential functions. Excitation spectra were recorded upon monitoring $^3P_0 \rightarrow {}^2F_2$ or $^3P_0 \rightarrow {}^3H_6$ transitions of the Pr^{3+} ion. All excitation and luminescence spectra were corrected for instrumental functions. Quantum yields were determined under excitation of the $^3P_2$ level of Pr^{3+} ion using an absolute method based on a specially modified integration sphere from GigHertz Optik in Zenith Teflon of 2 in. in diameter.[32] The detailed experimental procedure was described previously.[33] Lifetime and absolute quantum yield values were calculated on the basis of three independent measurements.

Zero-field-cooled (ZFC) and field-cooled (FC) magnetic susceptibility data were collected under an applied field of 0.1 T in the temperature range of $T = 5-400$ K using a Quantum Design vibrating sample magnetometer. Field-dependent isothermal magnetization measurements were performed at $T = 5$ K under the applied field varying between −2 and +2 T. The obtained values were corrected for the diamagnetic contributions of the sample holder, the low-temperature varnish, and ionic core diamagnetism.

Results and Discussion

Crystal Structure. A suitable model has been found by both *DICVOL06* and *ITO12* corresponding to a *C*-centered monoclinic unit cell ($a = 16.841$ Å, $b = 11.792$ Å, $c = 15.906$ Å, $\beta = 108.512°$, and FOM = 15.4). An additional reflection condition ($hk0$): $h + k = 2n$ corresponds to one of the space groups Cc or $C2/c$. Our choice of the centrosymmetric space group $C12/c1$ was based on the subsequent successful refinement of the structure. The asymmetric space group Cc has also been tested. However, the atomic deviations of all atoms from their positions in the centrosymmetric model were less than one standard deviation. Hence, the average crystal structure of $Pr_2(MoO_4)_3$ is described by the model previously derived for $La_2(MoO_4)_3$ (see Table 1 for structure refinement data for $Pr_2(MoO_4)_3$).[34] The unit cell comprises 26

(30) Petčíček, V.; Dušek, M.; Palatinus, L. *JANA2006*; The Crystallographic Computing System, Institute of Physics: Praha, Czech Republic, **2006**.

(31) Brandenburg, K. *DIAMOND*, version 2.1c; Crystal Impact GbR: Bonn, Germany, **1999**.

(32) Gumy, F. Patent application PCT/IB2007/054187, **2007**.

(33) Aebischer, A.; Gumy, F.; Bünzli, J.-C. G. *Phys. Chem. Chem. Phys.* **2009**, *11*, 1346.

(34) Jeitschko, W. *Acta Crystallogr., Sect. B: Struct. Sci.* **1973**, *29*, 2074–2081.

Table 2. Structural Parameters and Derived Fourier Amplitudes

	harmonics[a]	x	y	z	U_{eq} (Å^2)
Pr[b]		1/2	1/4	0.8807(2)	0.0077(2)
	s, 1	−0.0125(1)	−0.0059(1)	0	
	c, 1	0	0	0.0087(3)	
Mo		1/2	1/4	0.3725(2)	0.0115(3)
	s, 1	0.0096(2)	0.0148(2)	0	
	c, 1	0	0	−0.0009(2)	
O1		0.3528(7)	0.0107(7)	0.2954(4)	0.021(2)
	s, 1	−0.0048(8)	−0.004(1)	0.0023(4)	
	c, 1	−0.014(1)	0.020(1)	0.0081(4)	
O2		0.7689(8)	0.3948(7)	0.0363(4)	0.023(2)
	s, 1	0.0078(9)	0.0341(8)	0.0081(4)	
	c, 1	0.008(1)	0.0063(8)	0.0018(4)	

[a] Harmonics are listed by term (s for sine, c for cosine) and order n. [b] The Crenel function with occupation parameter $o = 2/3$ is used for Pr ($x_4^0 = 0.5$).

independent atoms on general positions requiring the refinement of 26 × 4 = 104 structural parameters (assuming isotropic displacement parameters for ions). In the superspace description,[13] the corresponding model requires 12 + 18n structural parameters, the second member giving the number of parameters of n harmonics for the description of displacive modulations. It is known that the use of the superspace model could reduce the number of refined parameters. Thus, the 3D commensurate approximation and (3 + 1) D model with superspace group $I2/b(\alpha\beta0)00$ and $\mathbf{q} = 2/3\mathbf{a}^* + 8/9\mathbf{b}^*$ were used to describe the crystal structure of $Pr_2(MoO_4)_3$. The distribution of Pr^{3+} was modeled by a Crenel function with the center of the Pr-atomic domain located at $x_4^0 = 0.5$ and an occupation parameter $o = 2/3$.[13] The background of the synchrotron and laboratory powder diffraction data was modeled by 9- and 12-coefficient polynomial functions, respectively. The profile was fitted using a pseudo-Voigt function. The scale factor, sample displacement, background, profile, lattice parameters, displacive modulation functions (the first-order Fourier amplitudes for Pr, Mo, and O; see Table 2), atomic coordinates, and isotropic displacement parameters were refined together during the final step. The refinement converged with reasonably low agreement factors ($R_p = 0.0492$, $wR_p = 0.0676$, $S = 2.04$), but a closer examination of the profile revealed that the positions of some of the low-angle reflections were not modeled accurately (Figure 2A). Therefore, we attempted to refine the components of the **q** vector, in order to investigate whether the structure could possibly be incommensurate. The preliminary refinement of the incommensurate model resulted in the first **q**-vector component within the doubled standard deviation being equal to 2/3. But the value, 0.88810(2), of the second component became irrational, slightly deviating from the value of 8/9. Therefore, only the second component of the **q** vector was allowed to vary during the final step. The refinement of the incommensurate model (Figures 3 and 4) resulted in better agreement factors ($R_p = 0.0481$, $wR_p = 0.0660$, $S = 1.99$) and better correspondence between the calculated and observed reflection positions (Figure 2B). The refined structural parameters are listed in Table 1.

As already mentioned, $Pr_2(MoO_4)_3$ belongs to the group of scheelite-related compounds with 1/3 of the crystallographic A-site positions being vacant. Five

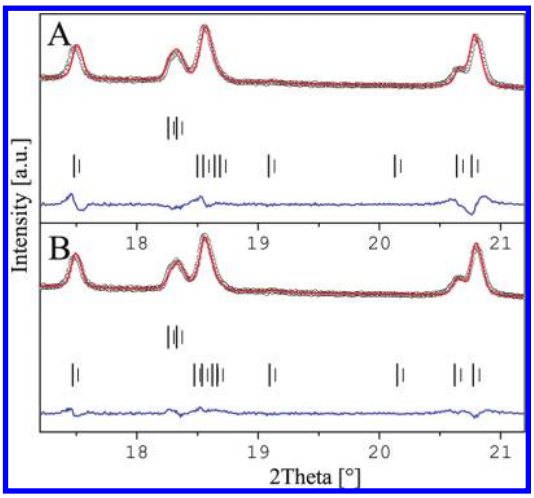

Figure 2. A portion of the low-angle laboratory X-ray powder diffraction data highlighting the difference between the fits obtained for the commensurate (A) and incommensurate (B) models. The upper and lower rows of reflection marks correspond to the average structure and satellite reflections, respectively.

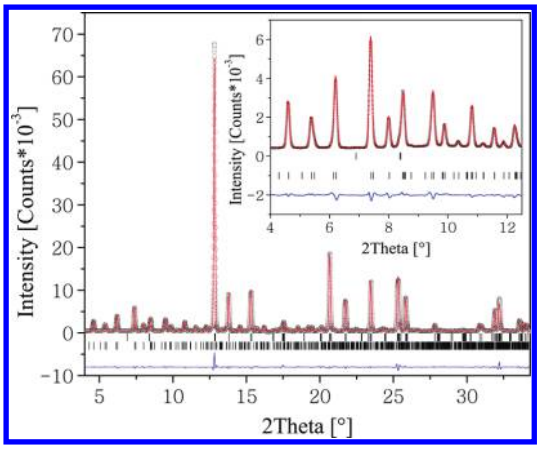

Figure 3. Rietveld refinement plot of the synchrotron X-ray powder diffraction data for $Pr_2(MoO_4)_3$. Space group: $I2/b(\alpha\beta0)00$. The observed, calculated, and difference intensities, and Bragg positions are shown. The upper and lower rows of reflection marks correspond to the average structure and satellite reflections, respectively. The inset shows a magnified portion of the low-angle X-ray diffraction data.

structural types with different ordering schemes of the cationic vacancies have been identified for these compounds.[34] $Pr_2(MoO_4)_3$ has been reported as a structural analog of $La_2(MoO_4)_3$.[35] The lattice of the $La_2(MoO_4)_3$-type structure is related to the (pseudo)tetragonal scheelite by the following transformation matrix:

$$\begin{pmatrix} a_m \\ b_m \\ c_m \end{pmatrix} = \begin{pmatrix} 3 & -1 & 0 \\ 0 & 0 & 1 \\ 3 & 0 & 0 \end{pmatrix} \begin{pmatrix} a_t \\ b_t \\ c_t \end{pmatrix}$$

where the subscript m represents the monoclinic and t the tetragonal unit cells. The vacancies in $La_2(MoO_4)_3$ are grouped in three clusters (Figure 5). The clusters are connected by symmetry operations of the space group $C12/c1$ when applied to the monoclinic unit cell. This

(35) Brixner, L. H.; Sleight, A. W.; Licis, M. S. *J. Solid State Chem.* **1972**, *5*, 247–249.

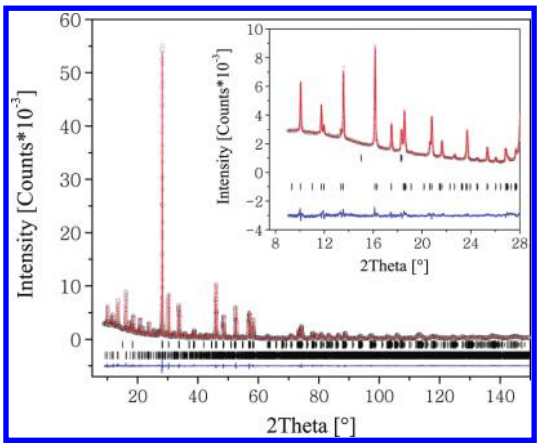

Figure 4. Rietveld refinement plot of the laboratory X-ray powder diffraction data for $Pr_2(MoO_4)_3$. Space group: $I2/b(\alpha\beta0)00$. The observed, calculated, and difference intensities and Bragg positions are shown. The upper and lower rows of reflection marks correspond to the average structure and satellite reflections, respectively. The inset shows a magnified portion of the low-angle X-ray diffraction data.

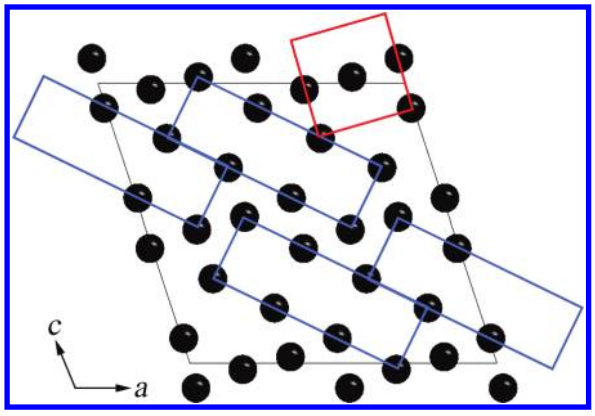

Figure 5. Vacancy ordering scheme for $La_2(MoO_4)_3$. Vacancy clusters are outlined with blue rectangles. The undistorted scheelite tetragonal unit cell is outlined with red.

cluster arrangement can be reproduced as a commensurately modulated structure within superspace group $I2/b(\alpha\beta0)00$ with $\mathbf{q} = 2/3\mathbf{a}^* + 8/9\mathbf{b}^*$ and a (pseudo)tetragonal unit cell.[8] The structure obtained for $Pr_2(MoO_4)_3$ is very similar to $La_2(MoO_4)_3$; however, this structure is incommensurately modulated since there is a small deviation of the second component of the **q** vector from the rational value (Table 1). This deviation creates faults in the Pr-vacancy distribution, regularly spaced along the *b* axis of the pseudotetragonal monoclinic lattice (Table 1). The distance between the two nearest faults can be estimated as follows: $d = \Delta/(\mathbf{q_c} - \mathbf{q_i})$, where Δ represents the width of the Pr-atomic domain, equal to 2/3, and $(\mathbf{q_c} - \mathbf{q_i})$ represents the difference between the commensurate and incommensurate **q** vectors. This formula yields $d \approx 450$ nm, which is equal to about 845 basic translations along the *b* axis of the monoclinic lattice of space group $I2/b(\alpha\beta0)00$. One of the faults is shown in Figure 6. It comprises a block of the vacancy clusters, each formed by four vacancies and located in the boundary separating two domains, each characterized by a $La_2(MoO_4)_3$-like structure. One can claim that the small deviation of the **q** vector from a rational value is a result of a regular nanosized domain distribution.

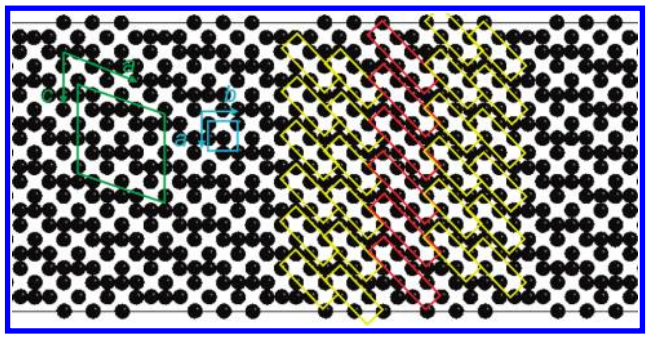

Figure 6. Vacancy ordering scheme observed in $Pr_2(MoO_4)_3$. The monoclinic unit cell is outlined in blue. The stacking of the regular vacancy blocks (in yellow) along the monoclinic *b* axis is interrupted by the defect vacancy blocks (in red).

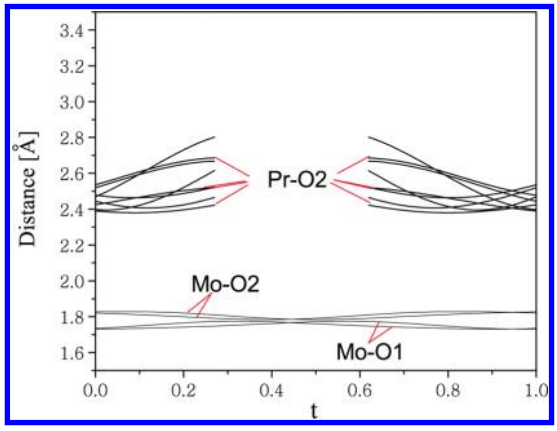

Figure 7. Distances between metal atoms and their surrounding O1 and O2 atoms plotted versus *t*.

It is further interesting to consider the first coordination spheres of the cation in $Pr_2(MoO_4)_3$ and compare them with $La_2(MoO_4)_3$. According to ref 34, the variation of the La−O distance among three different LaO_8 polyhedra is equal to Δ(La−O) = 0.126 Å, with very close average La−O distances (2.5198, 2.5202, and 2.5201 Å). The Mo−O distance varies between 1.73 and 1.82 Å, and the average of the Mo−O distance among five different MoO_4 tetrahedra varies between 1.771 and 1.781 Å. This confirms that there is no significant distortion of MoO_4 tetrahedra. In all three polyhedra, the coordination of La is also essentially the same, the first coordination sphere of each La^{3+} being surrounded by eight O^{2-} ions. The polyhedra are not significantly distorted. Figure 7 shows the variation of Pr−O distance values in $Pr_2(MoO_4)_3$ with the parameter *t*. Evidently, the spread of Pr−O distances is wider in comparison to the La−O ones. Indeed, according to the figure, the coordination number (CN) of Pr tends to vary between 7 + 1 and 8. On one hand, the variation in the Pr-valence state could account for the observed phenomenon. However, as will be proved by the magnetic and optical data analyses, there is no significant variation in the Pr-valence state. On the other hand, a decrease in the ionic radius of lanthanides reduces the tendency of the ion to retain a higher CN and to form rigid polyhedra. Therefore, the larger variation observed in the Pr−O distances as compared to the La−O ones can be explained by the difference in ionic radii of Pr^{3+} (1.126 Å, CN = 8) and La^{3+} (1.16 Å, CN = 8).

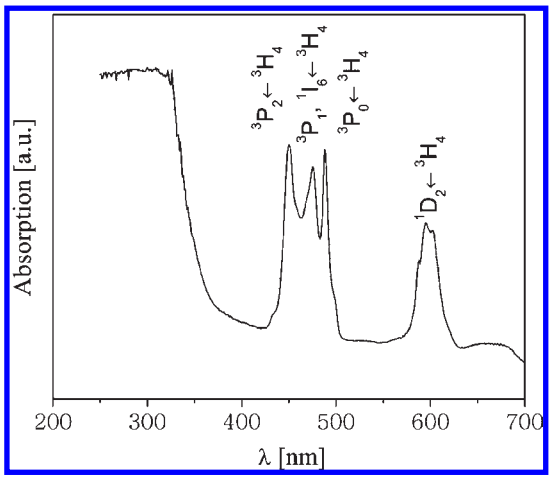

Figure 8. Absorption spectrum of $Pr_2(MoO_4)_3$.

Figure 7 gives the opportunity to evaluate the surroundings of the $Pr_2(MoO_4)_3$ vacancies. The distance between a vacancy and the closest O^{2-} ions tends to increase in comparison to the one between Pr^{3+} and O^{2-}. This is somewhat expected and indeed observed in $La_2(MoO_4)_3$.[34] The coordination number 7 of the vacancies in $Pr_2(MoO_4)_3$ is lower than that in $La_2(MoO_4)_3$, which is 8. It is significant that only CN = 8 is observed in the interdomain boundary. This fact is consistent with larger vacancy clusters appearing in the interdomain fault (Figure 6).

All of the known room-temperature structures of molybdates and tungstates with general composition $A_2(XO_4)_3$ (A = RE) belong to three different structure types: $La_2(MoO_4)_3$, $Eu_2(MoO_4)_3$, and $Sc_2(WO_4)_3$.[36] The former two can be derived from the parent scheelite structure and differ in their cationic vacancy ordering schemes.[13] The latter one belongs to the $Al_2(WO_4)_3$ structure type. The selection of the structure type depends on the ionic radius, R, of the RE ion.[36] Thus, molybdates with a larger ionic radius of the lanthanide adopt the $La_2(MoO_4)_3$ type ($R(La^{3+})$ = 1.16 Å) and CN(La) = 8. The decrease of the ionic radius leads to the $Eu_2(MoO_4)_3$ type ($R(Eu^{3+})$ = 1.066 Å). The CN of Eu is still equal to 8. In the $Sc_2(WO_4)_3$ type ($R(Sc^{3+})$ = 0.745 Å), the CN of Sc reduces to 6. Probably, the ionic radii of RE can also account for the different vacancy ordering schemes of the $La_2(MoO_4)_3$- and $Eu_2(WO_4)_3$-type compounds. The exact relation between these two parameters is however difficult to establish so far with the present experimental data.

Optical Properties. The diffuse absorption spectrum of $Pr_2(MoO_4)_3$ presents narrow bands at 450, 475, 485, and 570−620 nm due to $^3P_2 \leftarrow {}^3H_4$, $^3P_1$, $^1I_6 \leftarrow {}^3H_4$, $^3P_0 \leftarrow {}^3H_4$, and $^1D_2 \leftarrow {}^3H_4$ transitions, respectively, along with a broad intense band in the UV range extending further into the visible (Figure 8). Absorption up to 330 nm is attributed to the band gap and occurs through excitation of electrons from the valence to the conduction band.[37] The band gap energy of 4.0 ± 0.1 eV has been calculated from the position of the absorption edge. The narrow bands at 430−500 nm and 570−620 nm are attributed to the light absorption via the f−f electronic transitions of Pr^{3+} and can be assigned to the $^3H_4 \rightarrow {}^3P_J$ (J = 0−2) and the $^1I_6$ and $^1D_2$ transitions, respectively. No wide absorption bands in the range of 300−570 nm and peaks around 330 and 395 nm, which could be attributed to Pr^{4+} ion, were found. This confirms that praseodymium ions of the molybdate occur only in a trivalent state.

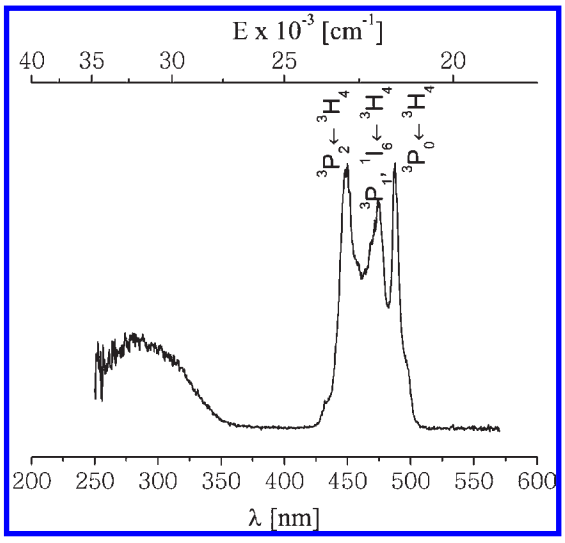

Figure 9. Excitation spectrum of $Pr_2(MoO_4)_3$ recorded at T = 295 K upon monitoring $^3P_0 \rightarrow {}^3F_2$ transition (649 nm).

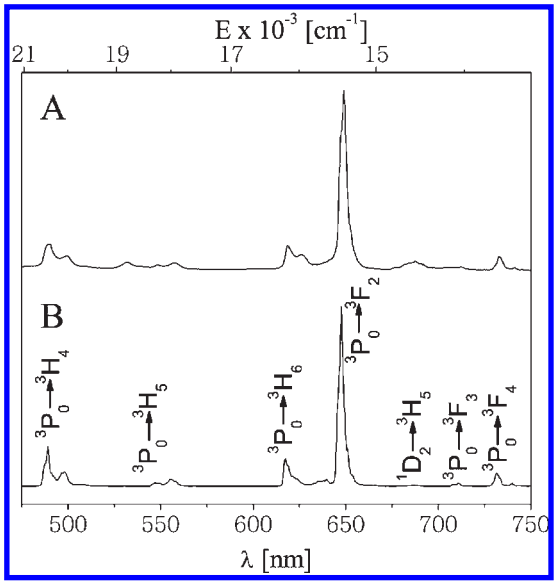

Figure 10. Emission spectra of $Pr_2(MoO_4)_3$ upon excitation of the Pr^{3+} ion ($^3P_2$ level, 450 nm) (A) at T = 295 K and (B) at T = 77 K.

Room-temperature excitation spectra (Figure 9) of the sample exhibits a broad band in the range of 250−350 nm along with more intense f−f electronic transitions of the Pr^{3+} ion in the visible range at 450 ($^3P_2 \leftarrow {}^3H_4$), 475 ($^3P_1$, $^1I_6 \leftarrow {}^3H_4$), and 485 ($^3P_0 \leftarrow {}^3H_4$) nm. It is worth mentioning that the excitation spectrum coincides well with the absorption one. Upon excitation into the $^3P_2$ level (450 nm) of the Pr^{3+}, praseodymium molybdate displays characteristic red luminescence from mainly $^3Pr_0$ to ^3H_J (J = 4−6) or ^3F_J (J = 2−4) levels, with the most intense band at 647.5 nm corresponding to the $^3P_0 \rightarrow {}^3F_2$ transition (Figure 10). Emission from the $^1D_2$ level is very weak

(36) Abrahams, S. C.; Bernstein, J. L. *J. Chem. Phys.* **1966**, *45*, 2745–2752.
(37) De Mello Donega, C.; Meijerink, A.; Blasse, G. *J. Phys. Chem. Solids* **1995**, *56*, 673–685.

Table 3. Position of the Bands and Integral Intensities of Pr^{3+} f−f Transitions (relative to $^3P_0 \rightarrow {}^3F_2$) in the Luminescence Spectra of $Pr_2(MoO_4)_3$ at 77 K

compound	$^3P_0 \rightarrow {}^3H_4$	$^3P_0 \rightarrow {}^3H_5$	$^3P_0 \rightarrow {}^3H_6$	$^3P_0 \rightarrow {}^3F_2$	$^1D_2 \rightarrow {}^3H_5$	$^3P_0 \rightarrow {}^3F_3$	$^3P_0 \rightarrow {}^3F_4$
integral intensity	0.33	0.08	0.17	1.00	0.01	0.02	0.08
λ, nm	489, 498	547, 555.5	617.5	647.5	687	708, 711	731, 740

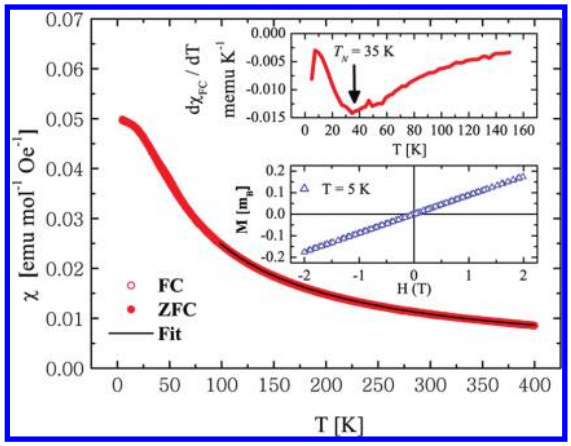

Figure 11. Temperature dependence of the FC and ZFC molar magnetic susceptibility of $Pr_2(MoO_4)_3$ measured under the applied magnetic field of $H = 0.1$ T. The inset shows the temperature derivative of the FC magnetic susceptibility ($d\chi_{FC}/dT$) variation with T and the isothermal magnetization $M(H)$ loop ($T = 5$ K, $-2\ T < H < 2$ T).

and presents less than 1% of the total integrated intensity (Table 3). Upon excitation into this level at 598 nm, no luminescence in the visible and emission in the near-infrared (NIR) range were detected. Very weak emission at 900−1100 nm due to the $^1D_2 \rightarrow {}^3F_4$ transition could be observed when excited into the $^3P_2$ level at 450 nm. Luminescence decays upon monitoring either $^3P_0 \rightarrow {}^3F_2$ (649 nm) or $^3P_0 \rightarrow {}^3H_6$ (619 nm) transitions, which are monoexponential functions with lifetime values being the same and equal to 10.1(2) μs. The absolute quantum yield of $Pr_2(MoO_4)_3$ measured under direct excitation into the $^3P_2$ level of Pr^{3+} was found to be only 0.092(1)%. The low luminescence can be caused by the concentration quenching via the efficient cross-relaxation process between closely settled Pr ions. Indeed, the refinement of the structure indicates that the Pr^{3+} ions in $Pr_2(MoO_4)_3$ are arranged in blocks extending along the c axis (Figure 6). The shortest distance between two blocks corresponds to the distance between two closest vacancies and is equal to $1/2(a_t + b_t + c_t)$ or ~6.99 Å (where a_t, b_t, and c_t are lattice parameters of the parent tetragonal cell). Within one block, the ions form a 2D network, where two closest neighbors are related by the symmetry operation 4_1 along the c axis. Hence, the distance between two closest Pr ions corresponds to the translation $1/2a_t + 1/4c_t$ or ~3.97 Å.

Magnetism. The temperature dependence of the molar magnetic susceptibility of $Pr_2(MoO_4)_3$ is presented in Figure 11. No difference between the FC and ZFC magnetic susceptibility values was observed. Above $T =$ 100 K, the FC magnetic susceptibility data of $Pr_2(MoO_4)_3$ were fitted to the Curie−Weiss formula:

$$\chi = \chi_0 + \frac{C}{T - \Theta} \qquad (1)$$

where χ_0 represents contributions of the Landau and ionic core diamagnetism and Pauli paramagnetism, T is temperature, and Θ refers to the Weiss constant and C to the Curie constant. The fitting of the data results in $\chi_0 = 1.14 \times 10^{-3}$ emu mol^{-1} Oe^{-1} (with a Pr^{3+}, Mo^{6+}, and O^{2-} ionic core diamagnetism contribution of 2.05×10^{-4} emu mol^{-1} Oe^{-1}), $C = 0.43 \times 10^{-3}$ emu mol^{-1} Oe^{-1}, and $\Theta = -39$ K. The latter indicates antiferromagnetic ordering of magnetic moments of Pr^{3+} ions ($4f^2$). The effective magnetic moment, $\mu_{eff} = 3.63\ \mu_B$, derived from the C value, is close to the theoretically predicted one for the free Pr^{3+} ion (3.54 μ_B). Thus, it can be concluded that, in the investigated oxide, the praseodymium ion is mainly presented in oxidation state +3.

The inset of Figure 11 shows the temperature derivative of the FC magnetic susceptibility ($d\chi_{FC}/dT$) used to determine the Néel temperature (T_N), which was found to be $T_N = 35$ K. Isothermal magnetization (M) measurements (inset of Figure 11) reveal no magnetic hysteresis and M saturation.

Conclusions

Praseodymium molybdate $Pr_2(MoO_4)_3$ has been synthesized, and its incommensurate crystal structure has been successfully described in the superspace approach, using superspace group $I2/b(\alpha\beta0)00$. The main structure motif of the material is similar to that of $La_2(MoO_4)_3$, but slightly different in terms of coordination of the rare-earth element: for La, CN = 8; for Pr, CN = 7 + 1 and 8. In addition, the crystals of $Pr_2(MoO_4)_3$ contain regularly spaced stacking fault defects accounted for by the incommensurate character of their structure. The defects separate nanosized domains. The incommensurate modulation of the cationic site occupation and displacive atomic modulations lead to a description of the structure in terms of interdomain faults. The origin of the defects and their regularity is not yet fully clarified, but it would be expected that, after some thermal treatment at elevated temperatures, the structure could become commensurate.

Emission characteristics of $Pr_2(MoO_4)_3$ were investigated in visible and NIR ranges. It has to be noted that the absorption spectrum of $Pr_2(MoO_4)_3$ and its strongest excitation band of 450 nm overlap significantly with that of modern GaN and GaInN-based blue LEDs (370−470 nm),[17] which have an excess of the blue and a lack of the red component. Moreover, the generation of the light from the red region ($^3P_0 \rightarrow {}^3F_2$ transition at 647.5 nm) using the blue region of the visible light is promising for white LEDs. The application of $Pr_2(MoO_4)_3$ in LEDs is however restricted due to its low quantum yield. Since no evidence for the presence of Pr^{4+} ions was found, the low emission quantum yield was attributed to concentration quenching between Pr^{3+} ions due to their high content (37 mol %). The latter can be decreased by substituting praseodymium with other rare-earth, alkaline-earth, or alkaline ions. This, in turn, may result in a change of the coordination environment and the valence state of Pr as well as optical properties.

It should be stressed that, due to the more accurate description of the local coordination and composition environment of the rare-earth ions, the superspace approach has an advantage over the 3D one in modeling the scheelite-related compounds. The superspace approach provides a better understanding of the relationship between their functional properties and composition. Thus, further development of the superspace approach to describe other scheelite family members seems to be promising.

Acknowledgment. We thank the Swiss National Science Foundation for financial support (Grants 20-105325/1 and 200021-109470/1) and Prof. Dr. Jean-Claude Bünzli for kindly allowing us to use the spectroscopic equipment of his group.

Supporting Information Available: A crystallographic information file is provided. This material is available free of charge via the Internet at http://pubs.acs.org.